

Sensing of Unexploded Ordnance With Magnetometer and Induction Data: Theory and Signal Processing

Yan Zhang, Leslie Collins, *Senior Member, IEEE*, Haitao Yu, Carl E. Baum, *Fellow, IEEE*, and Lawrence Carin, *Fellow, IEEE*

Abstract—We consider the detection of subsurface unexploded ordnance via magnetometer and electromagnetic-induction (EMI) sensors. Detection performance is presented, using model-based signal processing algorithms. We first develop and validate the parametric models, using both numerical and measured data. These models are then applied in the context of feature extraction, and the features are processed via two signal-processing algorithms. The detection algorithms are discussed in detail, with comparisons made based on performance with measured magnetometer and EMI data.

Index Terms—Induction, magnetometer, parametric model, sensing, signal processing, unexploded ordnance.

I. INTRODUCTION

AN UNEXPLODED ordnance (UXO) is a device that did not function as designed: the ordnance did not explode upon impact. Typically UXO can be found at many depths and orientations, depending upon their size, impact velocity, and angle of entry. Since these targets are buried, they represent minimal danger to sensors situated above the surface (after any existing surface UXO are cleared), and therefore such surface-based sensors as magnetometers and electromagnetic induction (EMI) are of significant interest for the UXO problem [1]–[5]. Radar is also of some interest [6], although radar has significant limitations in the context of sensing deeply buried UXO, due to wave attenuation in the soil.

Excavation of UXO is a very costly and dangerous endeavor, due to the care that must be taken to avoid explosion while digging, and because of the large number of false alarms declared with conventional processing approaches. Consequently, it is important to note that there is *not* a need for real-time signal processing in the context of the UXO problem. Since the targets are relatively benign as viewed on the surface (*vis-à-vis* landmines [7], [8]), the magnetometer and EMI data can be collected carefully and processed subsequently in the laboratory. Ideally, time (even extended time) spent in the laboratory carefully processing the data may reduce the *total* time and cost required for cleanup, through a reduction in the false-alarm rate (minimizing unnecessary excavation) and via an increased probability of detection.

A magnetometer senses changes in the observed background magnetic field of the earth, due to ferrous targets. It is well

known that the spatially dependent magnetometer signal is well modeled via a simple magnetic-dipole [9]. Therefore, in the context of model development, we direct our attention to EMI sensors. We extend the static magnetometer dipole model to the case of a frequency-domain EMI system. In the limit of vanishing frequency, the EMI model reduces to the aforementioned static model appropriate for a magnetometer. If desired, the EMI magnetic-dipole model can be expressed in the time domain as well, via an analytic Fourier transform.

We have demonstrated previously [1], [9] that the frequency- or time-dependent EMI signatures of simple conducting and ferrous targets can be expressed in terms of a dipole magnetization tensor (or dyadic), parametrized via magnetic singularities that exist along the imaginary axis of the complex frequency plane. These magnetic singularities represent a generalization of the singularity-expansion method (SEM) developed by Baum [10]; SEM has previously been applied primarily in the context of radar. In particular, the imaginary resonant frequencies of the EMI modes correspond, in the time domain, to the well-known damped-exponential EMI signatures of conducting/ferrous targets. Given the magnetization tensor of a particular target, as well as the excitation (incident) magnetic field, one can compute the associated time- or frequency-dependent EMI dipole moments. For UXO, which are often rotationally or near-rotationally symmetric, the dipoles are directed along and orthogonal to the target axis [1].

In this paper we extend the EMI magnetic-dipole model to the case of complex targets, such as UXO. It is demonstrated that the simple magnetic-dipole model discussed above can be extended readily to the case of complex targets, by considering *multiple* offset frequency-dependent magnetic dipoles, associated with various parts of the target. For example, in the context of a UXO, magnetic dipoles may be used to represent localized firing rings or fins on the ordnance, while distinct and spatially separated dipoles are used to represent the UXO's main body (or other components). After developing this extension of the EMI model, validation is performed using numerically generated data for canonical targets, as well as with measured data for actual ordnance.

We then demonstrate how the magnetometer and EMI models can be applied in the context of processing measured data, for UXO detection. In particular, we demonstrate that magnetometer data is relatively effective in localizing buried ferrous targets (most UXO are ferrous, as are many false targets). While information extracted from magnetometer data is typically insufficient for classification (distinguishing UXO from ferrous clutter), it is very important in constraining the

Manuscript received May 20, 2002; revised December 30, 2002.

Y. Zhang, L. Collins, H. Yu, and L. Carin are with the Department of Electrical and Computer Engineering, Duke University, Durham, NC 27708-0291 USA.

C. E. Baum is with the Air Force Research Laboratory, Directed Energy Directorate, Kirtland Air Force Base, Albuquerque, NM 87108 USA.

Digital Object Identifier 10.1109/TGRS.2003.810922

inversion of EMI data. In this context, “inversion” implies extraction of magnetometer and EMI model parameters, based on measured data. The EMI model has many parameters (e.g., dipole resonant frequencies, dipole orientation, dipole depth, etc.), and therefore there are often many local minima in the inverted model parameters. Much of this uncertainty can be removed by constraining the EMI inversion based on, for example, the target depth and location implied by the magnetometer data.

Once the model parameters are extracted from the measured data, the next stage is classification. We have formulated this as a binary problem, deeming the data to be associated with a UXO or non-UXO target (clutter)—it is typically too difficult to distinguish *between* different UXO types. Often false targets can appear very similar to a UXO, as viewed by the sensors. False targets are generated by, for example, components that are removed from the ordnance on impact (e.g., fins) as well as from ordnance that *did* explode on impact.

We consider several techniques for processing the extracted magnetometer and EMI model parameters. For example, we examine a likelihood ratio in which it is assumed that the variation in the model parameters (based on variation in the ordnance and/or perturbations to the UXO caused by impact) can be described via a multivariate Gaussian distribution [11]. The use of a Gaussian distribution is motivated by a desire for simplicity, rather than by an *a priori* expectation that such a model is physically motivated. Therefore, we also consider a support vector machine (SVM) classifier [12], for which no assumptions are required concerning the underlying statistics of the data. Results are presented using such classifiers, based on measured data from actual former bombing ranges. The results are parametrized in terms of receiver operating characteristics (ROCs), which quantify the probability of detection as a function of the false-alarm rate (FAR).

The remainder of the paper is organized as follows. In Section II we discuss the models developed for parameterization of the magnetometer and EMI data, with a focus on frequency- and time-domain EMI sensing of complex targets. The use of these models to extract parameters (features) from measured data is discussed in Section III, wherein we examine the use of magnetometer data to constrain inversion of the EMI data (constituting joint inversion of magnetometer and EMI data). The classification algorithms are discussed in Section IV, with example results presented in Section V. The research is summarized and conclusions are drawn in Section VI.

II. MAGNETOMETER AND EMI MODELS

A. Magnetometer Model

For sensors sufficiently distant from the target (relative to the target dimensions), the magnetic vector potential may be represented approximately as [13]

$$\mathbf{A}(\mathbf{r}) = \frac{\mu_o}{4\pi} \nabla \frac{1}{R} \times \mathbf{m} = \frac{\mathbf{m} \times \mathbf{R}}{R^3} \quad (1)$$

where \mathbf{m} is the magnetic dipole moment and \mathbf{R} is the vector from the target center to observation point ($R = |\mathbf{R}|$, $\mathbf{r} =$

\mathbf{R}/R). The associated magnetic field is expressed as $\mathbf{H} = (\mu_o/2\pi)\mathbf{m} \cdot \mathbf{r}/R^3$. The dipole approximation in (1) has been applied widely in the context of analyzing magnetometer data for sensing buried UXO [1], [2], [4], [5], and the accuracy of the magnetic-dipole model fit to measured data is often excellent. Therefore, in the context of the magnetometer data considered here, we assume that the spatially dependent magnetometer data may be represented accurately in terms of this dipole-magnetic model. In particular, the magnetometer field (usually one field component, normal to the interface) is measured as a function of position on the surface, and fit to the model in (1). The parameters one may extract with this model are the target depth, the magnetic-dipole orientation (not to be confused with the ordnance direction), and the goodness of fit (GOF) between the spatially dependent measured data and the representation in terms of the dipole model. These parameters are given further discussion when considering feature extraction and classification, in Sections III and IV.

B. Simple EMI Magnetic-Dipole Model

The EMI response of simple targets has been represented in terms of a frequency (time) dependent magnetic dipole, constituting a generalization of the magnetometer model. In particular, the magnetic dipole moment \mathbf{m} of a target is represented as $\mathbf{m} = \mathbf{M} \cdot \mathbf{H}^{\text{inc}}$ where \mathbf{H}^{inc} represents the incident (excitation) magnetic field and \mathbf{M} is a tensor that relates \mathbf{H}^{inc} to \mathbf{m} . For a UXO with axis along the z direction, we may express the magnetization tensor as [1]

$$\mathbf{M}(\omega) = \mathbf{z}\mathbf{z} \left[m_z(0) + \sum_k \frac{\omega m_{zk}}{\omega - j\omega_{zk}} \right] + (\mathbf{x}\mathbf{x} + \mathbf{y}\mathbf{y}) \left[m_p(0) + \sum_i \frac{\omega m_{pi}}{\omega - j\omega_{pi}} \right] \quad (2)$$

where \mathbf{z} is a unit vector in the z direction, and \mathbf{x} and \mathbf{y} correspond to orthogonal unit vectors, each perpendicular to \mathbf{z} . The terms $m_z(0)$ and $m_p(0)$ account for the induced magnetization produced for ferrous targets (valid down to static magnetic-field excitation, $\omega \rightarrow 0$), and the terms in the summations account for the frequency-dependent character. It is important to note that an EMI sensor operating down to zero (or a very low) frequency is distinct from a magnetometer, since the excitation magnetic fields are different in these two cases: for a magnetometer the target is excited by the earth's magnetic field, while for the very low frequency EMI sensor the excitation fields are generally constituted by a loop source. Note in (2) the poles at imaginary frequencies $j\omega_{zk}$ and $j\omega_{pi}$, these corresponding to the magnetic singularities that generalize the SEM method to EMI frequencies [1], [10]. For simple targets, typically we only require the first term in each sum, representative of the principal dipole mode along each of the principal axes.

Given the excitation magnetic fields \mathbf{H}^{inc} , from which we obtain \mathbf{m} using (2), the associated magnetic vector potential is computed using (1). If we assume that the EMI source responsible for \mathbf{H}^{inc} can be represented, as seen from the target, as a magnetic dipole with moment \mathbf{m}_s , then $\mathbf{H}^{\text{inc}} = \mathbf{r}_{st}(\mu_o/2\pi)(\mathbf{m}_s \cdot \mathbf{r}_{st}/R^3)$, where \mathbf{r}_{st} is a unit vector directed

from the source to the target center, with this distance represented by R ($|\mathbf{r}_{st}| = R$). If we assume that the source and observer coils are colocated (or near colocated), then the total magnetic field observed at the sensor \mathbf{H}^{rec} is represented by

$$\mathbf{H}^{\text{rec}}(\omega) \propto \frac{\mathbf{r}_{st}}{R^6} \mathbf{r}_{st} \cdot \mathbf{U}^T \cdot \mathbf{M} \cdot \mathbf{U} \cdot \mathbf{r}_{st} \quad (3)$$

where the proportionality constant depends on the strength of the dipole source \mathbf{m}_s and the characteristics of the receiver. If the signal is received (measured) with a small coil [13], then we measure that component of (3) along the coil axis. The 3×3 unitary matrix \mathbf{U} rotates the fields from the coordinate system of the sensor to the coordinate system of the target (the \mathbf{x} , \mathbf{y} , \mathbf{z} coordinate system in (3) is defined by the orientation of the target), and \mathbf{U}^T , which is the transpose of \mathbf{U} , transforms the dipole fields of the target (in the \mathbf{M} coordinate system) back to the coordinate system of the sensor. Clearly the matrix \mathbf{U} contains information about the target orientation (the angles of the target θ and ϕ with respect to the sensor coordinate system).

C. Extension of the EMI Dipole Model

The model discussed in Section II-B is adequate for relatively simple targets with dimensions small relative to the target-sensor distance. Note, for example, that the model in Section II-B implies that the EMI response is identical as observed from both ends of the target (i.e., from both ends of the target axis z). This is true for a cylinder, for example, but not in general for a UXO.

We also note that (2) does not explicitly define the physical position at which the target magnetic dipole is located. Implicitly, the dipole is located at or near the target center (or the center of mass). This motivates our extension of the model to more-complex targets. Rather than employing a single set of colocated dipoles, as in (2), we apportion a *set* of dipoles to *distinct* physical locations on the target, corresponding to distinct parts of the target. For example, many UXO are actually composites of multiple metal parts and, ignoring the coupling of current between these parts, each component is accorded its own set of magnetic dipoles.

We generalize the model in (2) as

$$\begin{aligned} \mathbf{M}(\omega) &= \sum_{n=1, N} \left\{ \mathbf{z}\mathbf{z} \left[m_z^n(0) + \sum_k \frac{\omega m_{zk}^n}{\omega - j\omega_{zk}^n} \right] + (\mathbf{x}\mathbf{x} + \mathbf{y}\mathbf{y}) \right. \\ &\quad \times \left. \left[m_p^n(0) + \sum_i \frac{\omega m_{pi}^n}{\omega - j\omega_{pi}^n} \right] \right\} \delta(\mathbf{r} - \mathbf{r}_n) \\ &= \sum_{n=1, N} \mathbf{M}_n(\omega) \delta(\mathbf{r} - \mathbf{r}_n) \end{aligned} \quad (4)$$

where \mathbf{r}_n represents the location of the n th set of dipoles. Note that we have assumed that the local coordinate system of each dipole set (\mathbf{x} , \mathbf{y} , \mathbf{z}) is the same, although this need not be true in general. Although the model in (4) appears to represent a significant escalation in complexity from (2), we note that in practice (for actual UXO) we typically only require a small number of terms N (typically $N = 1$, as in Section II-B, or $N = 2$). This is demonstrated in Section V.

We must also augment the expression in (3), from which we compute the composite received magnetic field. If we define \mathbf{r}_{sn} as a vector from the source to the location of dipole element n , then (3) now becomes, using (4),

$$\mathbf{H}^{\text{rec}}(\omega) \propto \sum_{n=1, N} \frac{\mathbf{r}_{sn}}{R_n^6} \mathbf{r}_{sn} \cdot \mathbf{U}^T \cdot \mathbf{M}_n \cdot \mathbf{U} \cdot \mathbf{r}_{sn}. \quad (5)$$

Since the target dimensions are often small relative to the interelement spacing, we typically approximate R_n as R , where R is the distance to the target center.

III. FEATURE EXTRACTION

A. Magnetometer Data

The models discussed in Section II are fit to measured data, and the associated model parameters are employed in the context of target detection (distinguishing UXO from non-UXO targets). The magnetometer data is typically measured on a two-dimensional grid, on the soil surface. The EMI data is similarly measured, while also being a function of time or frequency, for time- or frequency-domain EMI systems, respectively.

The magnetometer model in (1) involves a small set of parameters: the magnetic-dipole strength and direction (respectively $|\mathbf{m}|$ and $\mathbf{m}/|\mathbf{m}|$), as well as the target location. These parameters are computed relatively easily via a simple gradient-search of the model parameters. Recall that computational speed is not a particularly important issue for this problem, and therefore genetic-algorithm (GA) search strategies [14] may be employed to avoid local minima, although this has not constituted a significant problem in the context of the magnetometer data.

B. EMI Model Fitting

The EMI models in (2)–(5) are far more sophisticated than the magnetometer model, reflecting the enhanced information content in the EMI data (*vis-à-vis* the magnetometer), but also leading to difficulties with local minima when performing parameter extraction from measured data. Typically the sensor only measures one EMI field component (typically normal to the interface), this complicating problems with local minima. To circumvent this problem to some extent, we utilize parameters from the magnetometer inversion to constrain the determination of EMI model parameters. In particular, we utilize the depth and cross-sectional position afforded by the magnetometer inversion as part of the initialization of the EMI inversion (the target location in the EMI search is initialized in the vicinity of the region dictated by the magnetometer inversion). With regard to the other parameters in the EMI model, the search range is constrained based on previous experience with previously observed data. For example the EMI resonant frequencies $\omega_{zk}^n/2\pi$ and $\omega_{pi}^n/2\pi$ typically range from a couple hundred to several thousand Hertz, and such a range is considered in the parameter inversion.

In the classification results based on measured magnetometer and EMI data, presented in Section V, we have employed the simpler EMI model in (2), due to a limitation of available training data. Ideally, in the context of the more-sophisticated model in (5), we would utilize available EMI data from known targets (so-called training data) to extract the parameters in

(5) for several known UXO. These parameters (for example the relative positions of the multiple sets of dipoles, defined by $\mathbf{r}_1 - \mathbf{r}_2$) would then be used to constrain the inversion of the numerous parameters characteristic of (5). For example, if we knew *a priori* the relative positions of the multiple dipoles, this information may be used to initialize the parameter search associated with (5).

Within the context of (2) and (3), we here assume that only one term is required in each sum. The parameters to be determined are the approximate target center (constrained via the magnetometer inversion), the target orientation (characterized by the unitary matrix \mathbf{U}), $m_z(0)/m_p(0)$ (for ferrous targets), m_{z1}/m_{p1} , and ω_{z1} and ω_{p1} . These parameters are determined via a multi-dimensional gradient search [15]. Since we typically only measure one field component, we often find multiple local minima. To circumvent this problem we consider numerous solutions for the model parameters, based on random initializations of the parameters in (2), apart from the target position (this constrained by the magnetometer inversion). We typically find that most of the initializations lead to the same minima, while there are also several additional but less frequently visited “stray” minima. The final parameters are taken as those that correspond to the minimum mean-square error between the measured and model data. We again emphasize that it is the lack of real-time processing requirements that allow such a painstaking, careful parameter search (manifested by multiple parameter initializations). This process is demonstrated on measured data in Section V.

IV. CLASSIFICATION ALGORITHMS

We consider two techniques for target classification, here defined as identifying a target as UXO or non-UXO, without requiring the identification of the particular UXO type. This corresponds to a binary-hypothesis test, where here hypothesis H_1 is associated with a UXO, and hypothesis H_0 corresponds to a non-UXO target. The first approach is based on a likelihood-ratio test [11] and the second is based on a new classifier termed a support vector machine (SVM) [12]. Both algorithms process the feature vector \mathbf{v} , composed of the model parameters extracted from the magnetometer and EMI data. The specific parameters used by the classifiers are discussed in Section V.

A. Likelihood Ratio

Assume that $p(H_1|\mathbf{v})$ and $p(H_0|\mathbf{v})$ represent the probability of hypotheses H_1 and H_0 , respectively, given the feature vector \mathbf{v} . The optimal classifier is based on the likelihood ratio

$$\frac{p(H_1|\mathbf{v})}{p(H_0|\mathbf{v})} \stackrel{H_1}{\underset{H_0}{\gtrless}} \lambda \quad (6)$$

where λ is a threshold. Using Bayes’ theorem [11], this can be represented as

$$\frac{p(\mathbf{v}|H_1)p(H_1)}{p(\mathbf{v}|H_0)p(H_0)} \stackrel{H_1}{\underset{H_0}{\gtrless}} \lambda \quad (7)$$

where $p(\mathbf{v}|H_1)$ and $p(\mathbf{v}|H_0)$ represent the likelihood of the feature vector \mathbf{v} under the two hypotheses, and $p(H_1)$ and $p(H_0)$ represent the associated prior probabilities of each hypothesis.

The priors $p(H_1)$ and $p(H_0)$ can be used to account for the fact, for example, that it is generally far more likely to encounter false targets than actual UXO. The challenge is to approximate the likelihoods $p(\mathbf{v}|H_1)$ and $p(\mathbf{v}|H_0)$. Let \mathbf{m}_1 and \mathbf{m}_0 represent the mean feature vectors under hypotheses H_1 and H_0 , respectively, with associated covariance matrices Λ_1 and Λ_0 . The simplest approximation to the densities $p(\mathbf{v}|H_{0,1})$ is $p(\mathbf{v}|H_{0,1}) \sim N(\mathbf{m}_{0,1}, \Lambda_{0,1})$, i.e., \mathbf{v} is represented under both hypotheses as a multivariate Gaussian random process. Under this hypothesis the likelihood ratio (6) becomes [11]

$$(\mathbf{v} - \mathbf{m}_0)^T \Lambda_0^{-1} (\mathbf{v} - \mathbf{m}_0) - (\mathbf{v} - \mathbf{m}_1)^T \Lambda_1^{-1} (\mathbf{v} - \mathbf{m}_1) \stackrel{H_1}{\underset{H_0}{\gtrless}} \lambda^* \quad (8)$$

where λ^* represents a modified form of the threshold. Given a set of feature vectors \mathbf{v} , variation of the threshold λ^* yields a variation in the probability of detection (Pd) and the probability of false alarm (Pfa, defined as the probability that a non-UXO target is declared a UXO) or false alarm rate (FAR, defined as the number of false alarms per square meter); the variation of Pd vs. Pfa or Pd vs. FAR is termed the receiver-operating characteristic (ROC) [11].

To implement the classifier in (8) we must *a priori* estimate the mean feature vectors \mathbf{m}_0 and \mathbf{m}_1 , and the covariance matrices Λ_1 and Λ_0 , with this accomplished using available “training” data. Training data consists of a set of magnetometer and EMI data for which “truth” is known (i.e., the data is known to be representative of a UXO or non-UXO target), and the associated extracted model parameters (constituting the feature vectors) are used to approximate the parameters needed for (8).

B. Support Vector Machine (SVM)

The likelihood-ratio test in (7) is optimal assuming that the underlying density functions $p(\mathbf{v}|H_1)$ and $p(\mathbf{v}|H_0)$ are correct [11]. The choice of representing these in terms of multivariate Gaussian density functions is motivated by algorithmic simplicity, not by *a priori* knowledge that such a statistical model is physically motivated or rigorously correct. Therefore, while the expression in (8) is algorithmically simple, there is no guarantee that performance will be optimal. However, it is very difficult to motivate or realize a more-sophisticated representation for the underlying density functions. This is a ubiquitous problem in attempting to perform classification based on target-dependent density functions.

To mitigate this shortcoming of the likelihood-ratio procedure, alternative classifiers have been developed. A particularly promising new classifier is the support vector machine (SVM) [12]. Note from (7) that any threshold λ divides the feature space characteristic of \mathbf{v} into regions associated with hypothesis H_1 , and other regions associated with hypothesis H_0 . Recognizing this feature-space segmentation as the final result of an optimal classifier, the SVM seeks to develop this feature-space partition directly, without explicitly defining the underlying density functions $p(\mathbf{v}|H_1)$ and $p(\mathbf{v}|H_0)$. Below we provide a brief summary of the SVM framework.

Based on structural-risk minimization principles, support vector machines (SVMs) have recently achieved remarkable success in pattern-recognition problems [12]. The SVM clas-

sifier constructs the maximum-margin hyperplane in feature space to distinguish between two pattern classes “+1” and “-1” (binary classifier). We assume that we are given a set of labeled training observations $T = \{(\mathbf{v}_1, y_1), (\mathbf{v}_2, y_2), \dots, (\mathbf{v}_L, y_L)\}$, with labels $y_i \in \{-1, +1\}$.

Let $\mathbf{x}_i = \varphi(\mathbf{v}_i)$ be the feature vectors obtained after a generally nonlinear feature mapping φ . If \mathbf{w} represents the vector normal to a hyperplane classifier in the space \mathbf{X} of \mathbf{x}_i , and b the distance of the origin of the coordinate system measured from the hyperplane, then we would like to have a margin of separation of at least $1/\|\mathbf{w}\|$ from the hyperplane to the nearest data point among \mathbf{x}_i

$$y_i[\langle \mathbf{w} \cdot \mathbf{x}_i \rangle + b] \geq 1, \quad \forall i = 1, \dots, L. \quad (9)$$

The expression $\langle \mathbf{w} \cdot \mathbf{x}_i \rangle$ represents an inner product between the vectors \mathbf{w} and \mathbf{x}_i .

We note that this can always be achieved by scaling the vector \mathbf{w} appropriately if the two classes are linearly separable in their feature space. It may be easily seen that in the event of such a scaling of \mathbf{w} , $1/\|\mathbf{w}\|$ is a measure of separation between the two classes due to the hyperplane. However, in practice there may not be a hyperplane that can separate the two classes completely, especially in the presence of noise. Consequently, we permit classification errors to exist in some of the labels declared by the SVM. In other words,

$$y_i[\langle \mathbf{w} \cdot \mathbf{x}_i \rangle + b] \geq 1 - \xi_i, \quad \forall i = 1, \dots, L \quad (10a)$$

and

$$\xi_i \geq 0, \quad \forall i = 1, \dots, L. \quad (10b)$$

Thus a classifier $\{\mathbf{w}, b\}$ which generalizes well can be found by controlling both the classification margin (via $\|\mathbf{w}\|$) and the number of training errors. This is achieved by minimizing the objective function

$$\tau(\mathbf{w}, \xi) = \frac{\|\mathbf{w}\|^2}{2} + \gamma \sum_{i=1}^L \xi_i \quad (11)$$

subject to constraints (10a) and (10b) for some constant $\gamma > 0$ determining the tradeoff between training errors and generalization capability. It is useful to observe that (11) is a quadratic programming problem with linear constraints. It can be solved using the method of Lagrange multipliers, and hence reduced to its dual formulation as illustrated in [12]:

$$\text{Max } W(\alpha) = \sum_{i=1}^L \alpha_i - \frac{1}{2} \sum_{i,j=1}^L \alpha_i \alpha_j y_i y_j \langle \mathbf{x}_i, \mathbf{x}_j \rangle \quad (12)$$

subject to

$$\gamma \geq \alpha_i \geq 0, \quad i = 1, \dots, L, \quad \text{and} \quad \sum_{i=1}^L \alpha_i y_i = 0. \quad (13)$$

We have used the SMO algorithm [12] to solve this constrained optimization problem to identify the optimal \mathbf{w} , b of

the hyperplane. Then the SVM classifier is obtained using $\mathbf{w} = \sum_{i=1}^L y_i \alpha_i \mathbf{x}_i$ so that

$$f(\mathbf{v}) = \text{sign} \left(\sum_{i=1}^L y_i \alpha_i \langle \varphi(\mathbf{v}), \varphi(\mathbf{v}_i) \rangle + b \right). \quad (14)$$

Those \mathbf{v}_i for which $\alpha_i > 0$ are called the support vectors. Thus, only the support vectors affect the final decision function of the SVM.

The function $K(\mathbf{v}, \mathbf{v}_i) = \langle \varphi(\mathbf{v}), \varphi(\mathbf{v}_i) \rangle$ is a nonlinear measure of similarity between the observations \mathbf{v} and \mathbf{v}_i , termed the kernel function. We note that if the kernel is given, then we do not need to compute $\varphi(\mathbf{v})$ explicitly. This property enables us to use an infinite-dimensional feature space \mathbf{X} for the purpose of classification.

V. EXAMPLE RESULTS

In this section we present several sets of results, to investigate model accuracy, the extraction of model parameters based on measured data, and finally classification results on measured magnetometer and EMI data collected at a former range. We begin by considering the accuracy of the EMI models in the frequency domain, based on data computed numerically via a finite-element model (FEM).

A. EMI Fitting to FEM-Generated Synthetic Data

An FEM model has been developed to analyze the frequency-domain EMI response of general conducting and ferrous targets [1]. The FEM model has been discussed in [1], and therefore here we focus on its applicability for validating the simpler, parametric EMI model discussed in Section II. We emphasize that while the FEM model is numerically rigorous and very accurate [1], it is inappropriate for use in the context of target classification, due to its computational expense. The model discussed in Section II is much simpler, and its parametric form plays an important role in the subsequent classification studies.

We consider a conducting cylinder of length 2.54 cm, diameter 2.54 cm, and conductivity $\sigma = 3 \times 10^7$ S/m. In addition, we consider a ring of inner radius 2.6 cm, outer radius 3.9 cm, thickness 5 mm, and conductivity $\sigma = 5 \times 10^6$ S/m. The targets are sensed via a simulated GEM-3 frequency-domain EMI sensor (this sensor has been developed by Geophex, Ltd., as described in [16]). The cylinder and ring are used to realize a composite target, as depicted in Fig. 1. The center of the sensor coils are positioned 12 cm from the center of the cylinder.

Our objective is to consider the fit of the parametric model in (2) and (3) to the FEM-computed EMI signature of the cylinder and ring alone. We then address the accuracy of the composite model of (4) and (5) in the context of the cylinder-ring composite target. In this test we first perform the model fit of the isolated targets, from which we extract the parameters required in (2). These same parameters are then used in the composite model of (4), but now the associated dipoles are positioned at the center of the cylinder and ring respectively (i.e., the magnetic dipoles associated with the ring and cylinder are offset with respect to each other, to reflect the respective positions of the corresponding target parts).

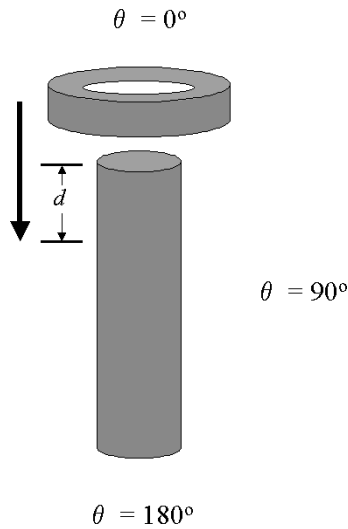


Fig. 1. Schematic of a conducting cylinder and ring, the two used to constitute a composite target. Also denoted is the coordinate system used to define the angle of observation θ . In the computations considered here the cylinder length and diameter are 2.54 cm; the ring is defined by an inner diameter of 2.6 cm, outer diameter 3.9 cm, and thickness 5 mm; the distance $d = 5$ mm; and the cylinder and ring conductivities are $\sigma = 3 \times 10^7$ S/m and $\sigma = 5 \times 10^6$ S/m, respectively.

In Fig. 2, we depict the in-phase and quadrature (real and imaginary, respectively) components of the computed voltage computed for the sensor, with the ring and cylinder in isolation. Results are shown with the coil axes aligned with the target axes (0°) and orthogonal to the target axes (90°). The solid curves represent the FEM computations and the points the model fits based on (2). Note that the entire frequency spectrum, real and imaginary parts, for *both* angles combined, is described by only four parameters (for each of the individual targets): m_{z1} , m_{p1} , ω_{z1} and ω_{p1} . This is a particularly simple case because the targets are nonferrous ($m_z(0) = m_p(0) = 0$). The model fit was performed using a gradient-descent search, based on data from both observation angles, 0° and 90° .

In Fig. 3, we now compare the rigorous, *coupled* FEM solution of the ring-cylinder composite, *vis-à-vis* the model fit in (4) and (5), using the model parameters extracted from the *individual* targets. In the model of (4) and (5) we employ a total of eight parameters (m_{z1} , m_{p1} , ω_{z1} , ω_{p1} , m_{z2} , m_{p2} , ω_{z2} , and ω_{p2}), and we utilize the known target-sensor orientations [i.e., we know the rotation matrix \mathbf{U} in (5)]. In Fig. 3, we show comparisons between the FEM and parametric models for angles 0° , 90° , and 180° . The parametric model, which here ignores coupling between the components, is generally in good agreement with the rigorous FEM computations, particularly for 90° . It is also important to note that the composite target appears different to the sensor as observed at 0° and 180° , due to the fact that the ring is not in the center of the cylinder. A single set of dipoles, as in the model of (2) and (3), does not capture these differences.

B. EMI Fitting to Measured UXO Data

The FEM study in the previous section provided a well-controlled setting for investigating the EMI modeling framework outlined in Section II. We now consider this model in the context of *measured* GEM-3 data, for an actual ordnance. In particular,

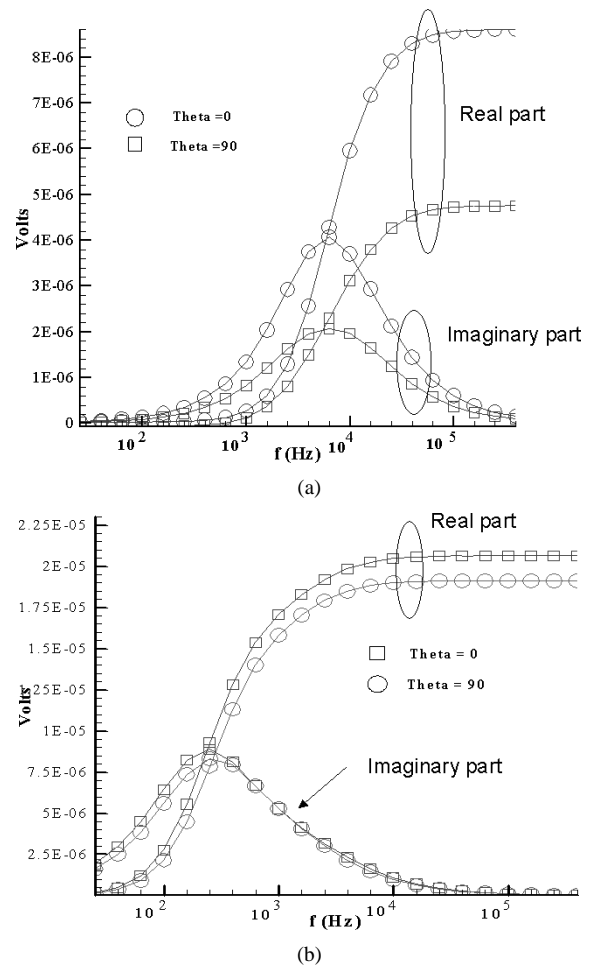


Fig. 2. Computed EMI voltage for ring and cylinder depicted in Fig. 1 (each in isolation), computed using the parameters of the GEM-3 sensor [16] at two angles of observation (see Fig. 1). The curves represent the FEM computations [1], and the points the model fit. The data used to produce the curves were computed at the same frequencies used for the model fit, and indicated with the points. (a) Ring. (b) Cylinder.

we consider an 81-mm mortar (Fig. 4), with all data measured in air (the measurements were performed in air for simplicity—as implied in Section II, the soil plays a minimal role in the EMI sensing of large, conducting ordnance, based on the data observed in this study). For very small ordnance the soil properties may become important, especially for highly conducting soils. In addition, for magnetic soils the effects of the soil are important. Such cases, which are rare but potentially important, would require a significant modification to the simple EMI model.

In Fig. 5, we present measured data (points) and the EMI fit based on the model in (4) and (5), for sensor angles of observation 0° , 90° , and 180° (see Fig. 4 for a definition of the coordinate system). Note the significant differences in the EMI signature as view along its axis from the top (0°) and from the bottom (180°), this motivating the composite model in (4) and (5). The model in (4) and (5) is valid at all frequencies and for all orientations (the latter accounted for via \mathbf{U}). The model fits for the z -directed EMI dipoles and p -directed EMI dipoles in (4) are determined separately. The former employs frequency-domain data from the top (0°) and bottom (180°) of the target, while the latter employs that from 90° . For example, in the context of the z -directed EMI dipoles, the parameters to be determined are

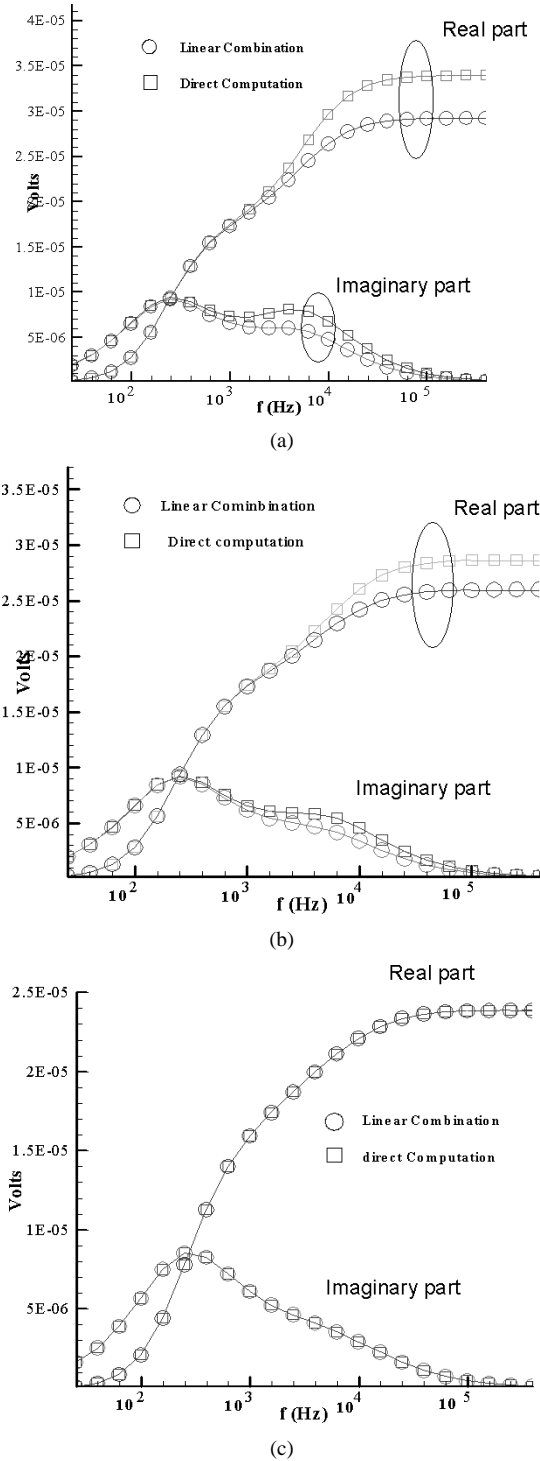


Fig. 3. EMI response of the composite ring-cylinder target in Fig. 1, as observed at three angles of observation. The squares denote the results of the direct FEM solution and the circles the model fit based on a dipole representation of each target part. The data used to produce these curves were computed at the frequencies associated with the points, denoted by squares and circles. (a) Observation angle 0° , (b) observation angle 180° , (c) observation angle 90° .

$m_z^n(0)$, m_{zk}^n , ω_{zk}^n , and r_n , for $n = 1$ and $n = 2$ and also $k = 1$ and $k = 2$. Although we must compute many model parameters, note that we have complex frequency-domain data available from three angles (Fig. 5) with which we perform the fit. To simplify the search, \mathbf{r}_1 is set to the center of the target, and there-

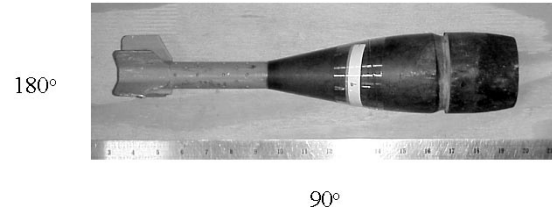


Fig. 4. Photograph of 81-mm ordnance, and the associated definition of the target-sensor angles of observation.

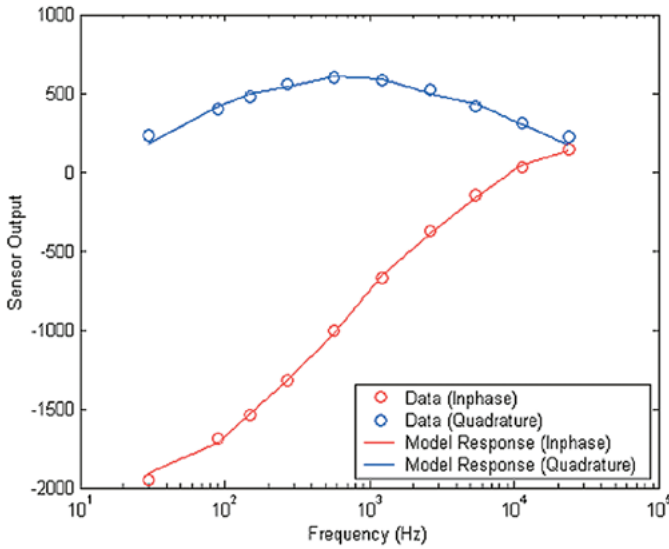
fore we need only find \mathbf{r}_2 with respect to the target center. The parameter fit was again performed via a gradient-based search, with satisfactory fits manifested as indicated in Fig. 5.

As a more-challenging test of the model, we utilize the parameters extracted in the context of Fig. 5—based on frequency-domain observations at three angles—to *predict* the complex frequency response at a fourth angle not observed when performing the model fit. Results are shown in Fig. 6 for GEM-3 measured data at 45° , with a comparison to the model of (4) and (5) based on parameters extracted from data at three separate observation angles. We see in Fig. 6 an encouraging comparison between the parametric model and the measured data. The results in Figs. 5 and 6 also demonstrate the generally strong aspect dependence to the frequency-domain EMI signatures of actual ordnance. However, it is important to emphasize that although the results in Figs. 5 and 6 show significant variation with orientation, each example is characterized by the same magnetization tensor \mathbf{M} , with the aspect-dependence of the signature characterized by \mathbf{U} . This implies that \mathbf{M} captures the underlying structure of the target itself, independent of orientation, and consequently the parameters of \mathbf{M} (not \mathbf{U}) are used in the classifiers.

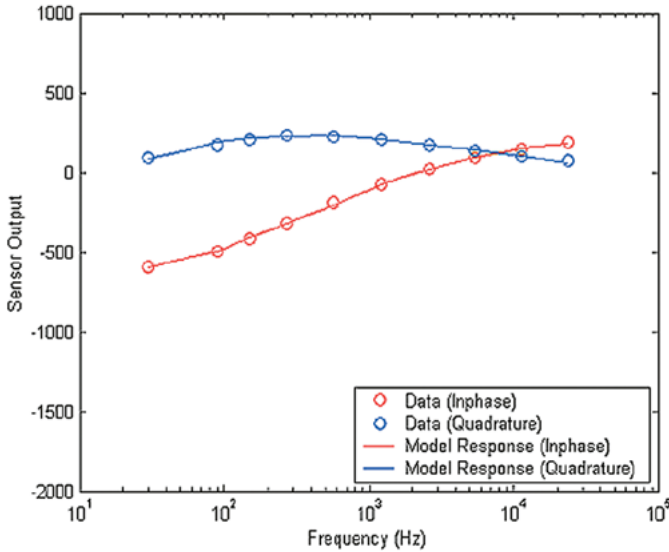
C. Classification Results Based on Measured “Field” Data

Geophex, Ltd. (producers of the GEM-3 EMI sensor [16]) collected data at Jefferson Proving Ground, a former military base in the United States. Both magnetometer and wideband GEM-3 EMI data were collected. The GEM-3 sensor was operated at the frequencies 90, 150, 330, 930, 2790, 8190, and 20 010 Hz. Initially a coarse survey was performed, and then a more-careful spatial grid of magnetometer and EMI data were collected about spatial regions where UXO-like targets appeared evident (based upon the energy in the magnetometer and EMI data—not based on the more-sophisticated algorithms employed subsequently, and discussed in Section IV). A total of 197 potential targets were surveyed carefully by Geophex, 16 of which were later revealed (by the sponsor) to be UXO, with the remaining 181 false targets (non-UXO). In this set of UXO were 60- and 81-mm mortars; 57-, 76-, 105-, 152-, and 155-mm projectiles; and a 2.75-in rocket.

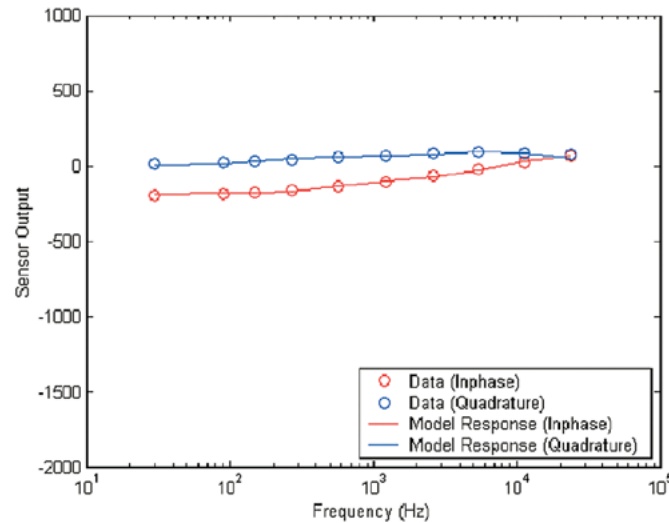
The classification results presented here are based on a “leave-one-out” study, implemented as follows. Let feature vector \mathbf{v}_0^n represent the n th feature vector associated with hypothesis H_0 (clutter class), with \mathbf{v}_1^n similarly defined for H_1 (target class). As indicated, we have 181 examples of \mathbf{v}_0^n and 16 examples of \mathbf{v}_1^n . We perform testing on *one* example of \mathbf{v}_1^n or \mathbf{v}_0^n , where here we denote \mathbf{v}_t as the particular feature vector tested. The classifier is trained using all available feature vectors \mathbf{v}_1^n and \mathbf{v}_0^n , *except* \mathbf{v}_t . After the classifier is trained, \mathbf{v}_t is



(a)



(b)



(c)

Fig. 5. GEM-3 measured data from the target in Fig. 4, as observed at three target-sensor orientations. The points reflect the measured data and the curves the model fit. The model parameters are the same for all orientations. (a) Observation angle 0° , (b) observation angle 180° , (c) observation angle 90° .

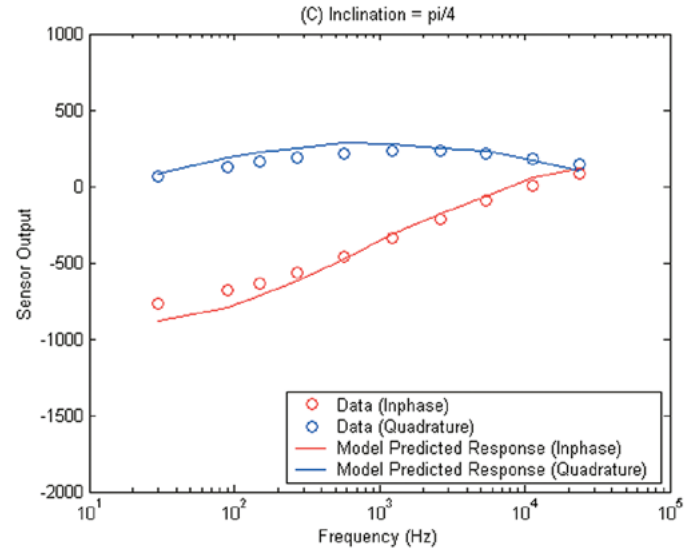


Fig. 6. GEM-3 measured data from the target in Fig. 4, as observed at 45° . The points reflect the measured data and the curves the model fit. The model parameters were extracted from the measured data in Fig. 5.

classified by it as being in H_1 or H_0 . We do this for all possible manifestations of \mathbf{v}_t (here 197) from which we obtain classification performance. This procedure constitutes a simple means of achieving classification statistics with a relatively small amount of data, while keeping the testing and training data distinct.

In the context of the Gaussian likelihood ratio in (8), the training data were used to estimate the means \mathbf{m}_0 and \mathbf{m}_1 , and covariance matrices Λ_1 and Λ_0 . Within the context of the SVM, the training data were used to constitute the labeled feature vectors $\{\mathbf{v}_n, y_n\}$, where $y_n = +1$ for UXO and $y_n = -1$ for non-UXO targets. The Gaussian likelihood-ratio ROC is computed by varying the threshold λ^* in (8). For the SVM we vary the *magnitude* of the vector $\mathbf{w} = \sum_{i=1}^L y_i \alpha_i \mathbf{x}_i$, which corresponds to shifting the position of the hyperplane, but not its orientation.

In the course of this study, it was determined that two GEM-3 frequencies, 930 Hz and 2790 Hz, were particularly useful for classification. This utility was dictated in large part by the characteristics of the sensor (e.g., the sensor realized minimal variation at these frequencies to such issues as sensor heating). Although we only were able to utilize data from two EMI frequencies, recall that we have data collected at multiple target-sensor positions (on a two-dimensional grid, on the surface). The sensor data was sampled at 20 cm in each of the two Cartesian directions in the grid, and the model fitting was performed using data collected over a $3 \text{ m} \times 3 \text{ m}$ area. Due to the small number of EMI frequencies employed, we were forced to simplify the EMI model discussed in Section II. In particular, we employed a single set of colocated magnetic dipoles, as in (2) and (3). Moreover, we defined

$$f_z(\omega) = m_z(0) + \sum_k \frac{\omega m_{zk}}{\omega - j\omega_{zk}} \quad (15a)$$

$$f_p(\omega) = m_p(0) + \sum_i \frac{\omega m_{pi}}{\omega - j\omega_{pi}} \quad (15b)$$

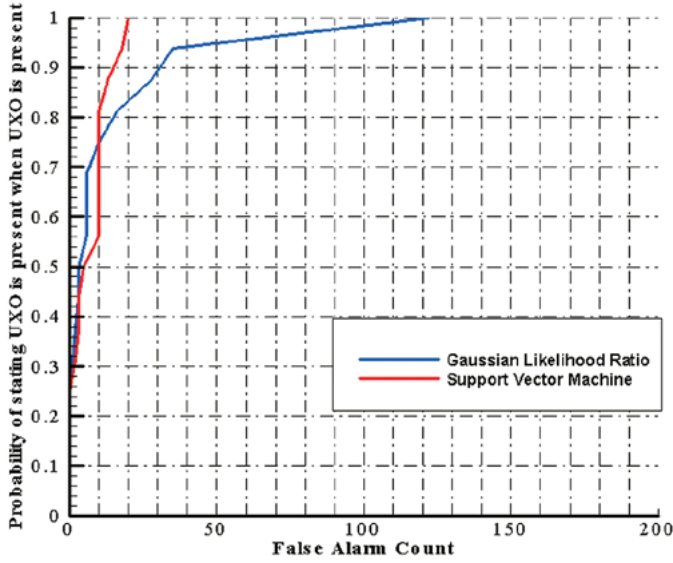


Fig. 7. Receiver operating characteristic (ROC) based on processing GEM-3 measured data. The computation of the EMI model parameters was constrained by the localization (position) information accrued from the magnetometer-based parameter estimation. Results are shown for the SVM and multivariate-Gaussian likelihood-ratio test.

where f_z and f_p account for the longitudinal and perpendicular magnetic-dipole components, at the two frequencies of interest, 930 Hz and 2790 Hz. Using these expressions in (3) yields the spatial variability of the EMI response (in terms of the unknown, and to be determined target orientation, characterized by \mathbf{U}). The particular EMI features employed are $\mathbf{v} = \{\text{Im}(f_p(\omega_1)), \text{Im}(f_p(\omega_2))/\text{Im}(f_p(\omega_2))\}$, where Im means “imaginary part of a complex number.”

We present a comparison of classifier performance in Fig. 7 for the Gaussian likelihood ratio and the SVM, where here we have employed a radial-basis-function SVM kernel [12]. These results are based on using the EMI features alone, although computation of these EMI parameters has been constrained, as discussed in Section III, by the results of the magnetometer parameter extraction (particularly the target location). We see from Fig. 7 that the two algorithms yield comparable classification performance, although the SVM results are slightly better. We note that the GEM-3 EMI sensor, in the context of relatively sophisticated classification algorithms, does an encouraging job of reducing most of the false targets.

As a comparison to the EMI-based classification, in Fig. 8 we present classification performance based on the magnetometer sensor alone (using only the features or parameters associated with the static magnetic-dipole model). Again the two algorithms yield comparable performance, and we note that the magnetometer classification performance is markedly worse than that shown in Fig. 7 for the wideband EMI sensor. The particular magnetometer feature employed was the magnetic-dipole direction ($\mathbf{m}/|\mathbf{m}|$). The magnetometer data were collected over the target using a 5-cm sampling rate in each Cartesian dimension, with the model fitting performed using data collected over a $3\text{ m} \times 3\text{ m}$ area. The similarity in the performance of the two classifiers, in Figs. 7 and 8, suggests that the multivariate Gaussian model for the likelihoods $p(\mathbf{v}|H_{1,0})$ is reasonable, since no un-

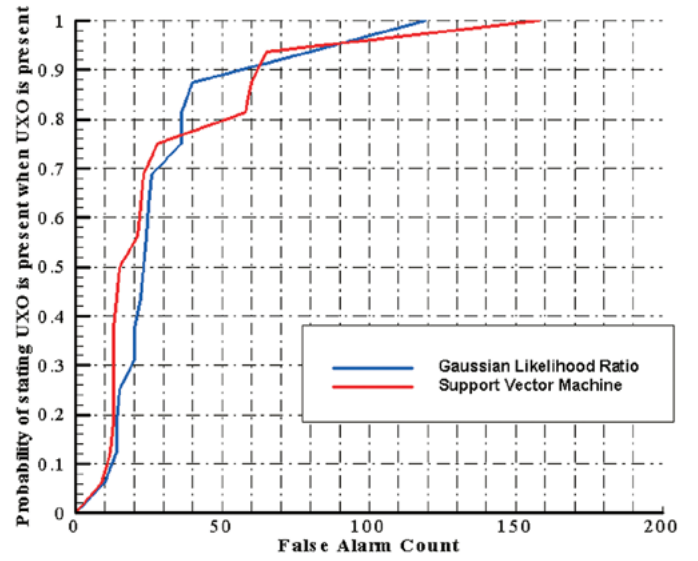


Fig. 8. As in Fig. 7, but here the classification results are based on parameters extracted from the magnetometer data alone.

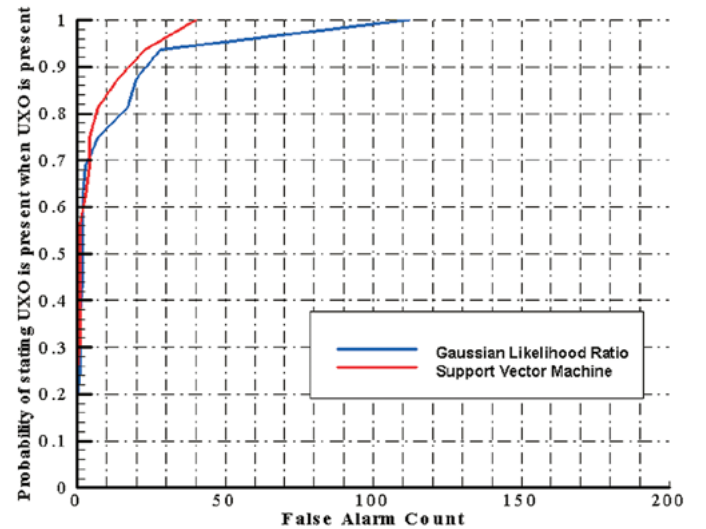


Fig. 9. As in Figs. 7 and 8, but now the classification results are based on feature vectors defined by both the magnetometer and EMI model parameters.

derlying statistical assumptions have been made in the context of the SVM.

The results in Fig. 7 are based on the EMI sensor, with parameter extraction constrained via the magnetometer data, and the results in Fig. 8 use the magnetometer parameters alone. In particular, the positional information provided by the magnetometer model fit was used in the initialization of the EMI-model parameter search. It is of interest to examine classification performance when we “fuse” the features from the EMI and magnetometer sensor (i.e., the cumulative feature vector \mathbf{v} is a concatenation of the features used in Figs. 7 and 8). The results found based on fusing the magnetometer and EMI features are presented in Fig. 9. Such fusion does not guarantee improved results *vis-à-vis* the performance of the individual sensors (Figs. 7 and 8), but we note in Fig. 9 a significant improvement in the detection probability when considering a small number of false alarms. In particular, for five false alarms, the

SVM results in Fig. 9 achieve a probability of detection of 0.7, while the EMI-alone results in Fig. 7 achieved a detection probability of 0.5. Nevertheless, it appears that best performance, for this limited dataset, is achieved by using the EMI features alone, with the EMI parameter extraction constrained by the parameters determined via the magnetometer data (target location).

VI. CONCLUSION

We have considered the problem of sensing buried UXO, based on the processing of magnetometer and wideband-EMI data. The classification algorithms have been based on processing features (parameters) extracted from parametric models for wideband EMI and magnetometer data. The models have been validated through consideration of numerical EMI data for canonical targets, as well as by using measured data from actual UXO. The EMI models represent an extension of the magnetic-dipole model widely applied in the context of magnetometer sensing. The wideband-EMI model employs a magnetization tensor, parametrized in terms of frequency-dependent magnetic dipoles. The frequency dependence is accounted for simply in terms of magnetic modes, characterized by imaginary resonant frequencies in the complex-frequency plane. Typically a small number of such modes are associated with a given target. We demonstrated that by considering offset magnetic dipoles, accounting for various components on a complex target, one can extend the simple magnetic-dipole model to the case of targets composed of multiple parts.

The parametric models have been employed in the context of processing measured magnetometer and EMI data, for buried UXO and non-UXO targets. Two classification algorithms have been considered, the two yielding comparable classification performance. The parameters extracted from the magnetometer data were used to constrain the wideband-EMI parameter extraction. On this limited dataset, the classification performance was best when these EMI model parameters were used in the classifier, with this performance markedly better than that found with the magnetometer parameters alone. With regard to fusing the magnetometer and EMI features (model parameters), in some regions (low false alarms) the fused results were superior, although in general the quality of the classification based on constrained EMI features appeared best.

Because of limitations with available training data, in the context of the EMI-based feature extraction, we only utilized a single set of *colocated* magnetic dipoles to characterize the EMI signature. However, we demonstrated in Section II the utility of a model based on composite, offset EMI magnetic-dipole moments. In future research we will examine whether this more-sophisticated model yields improved classification performance, assuming the presence of a more-extensive training data.

REFERENCES

- [1] L. Carin, H. Yu, Y. Dalichaouch, A. R. Perry, P. V. Czipott, and C. E. Baum, "On the wideband EMI response of a rotationally symmetric permeable and conducting target," *IEEE Trans. Geosci. Remote Sensing*, vol. 39, pp. 1206–1213, June 2001.
- [2] N. Geng, C. E. Baum, and L. Carin, "On the low-frequency natural response of conducting and permeable targets," *IEEE Trans. Geosci. Remote Sensing*, vol. 37, pp. 347–359, Jan. 1999.

- [3] H. H. Nelson and J. R. McDonald, "Multisensor towed array detection system for UXO detection," *IEEE Trans. Geosci. Remote Sensing*, vol. 39, pp. 1139–1145, June 2001.
- [4] S. J. Hart, R. E. Shaffer, S. L. Rose-Pehrsson, and J. R. McDonald, "Using physics-based modeler outputs to train probabilistic neural networks for unexploded ordnance (UXO) classification in magnetometry surveys," *IEEE Trans. Geosci. Remote Sensing*, vol. 39, pp. 797–804, June 2001.
- [5] C. V. Nelson, C. B. Cooperman, W. Schneider, D. S. Wenstrand, and D. G. Smith, "Wide bandwidth time-domain electromagnetic sensor for metal target classification," *IEEE Trans. Geosci. Remote Sensing*, vol. 39, pp. 1129–1138, June 2001.
- [6] C.-C. Chen and L. Peters, Jr., "Buried unexploded ordnance identification via complex natural resonances," *IEEE Trans. Antenna Propagat.*, vol. 42, pp. 1645–1654, Nov. 1997.
- [7] T. P. Montoya and G. S. Smith, "Land mine detection using a ground-penetrating radar based on resistively loaded Vee dipoles," *IEEE Trans. Antenna Propagat.*, vol. 47, pp. 1795–1806, Dec. 1999.
- [8] C. T. Schroder and W. R. Scott, Jr., "A finite-difference model to study the elastic-wave interactions with buried land mines," *IEEE Trans. Geosci. Remote Sensing*, vol. 38, pp. 1505–1512, July 2000.
- [9] C. E. Baum, Ed., *Detection and Identification of Visually Obscured Targets*. New York: Taylor and Francis, 1998.
- [10] C. E. Baum, "The singularity expansion method," in *Transient Electromagnetic Fields*, L. B. Felsen, Ed. Berlin, Germany: Springer-Verlag, 1976, ch. 3, pp. 129–179.
- [11] H. L. Van Trees, *Detection, Estimation, and Modulation Theory*. New York: Wiley, 1968–1971.
- [12] N. Cristianini and J. Shawe-Taylor, *An Introduction to Support Vector Machines: And Other Kernel-Based Learning Method*. Cambridge, U.K.: Cambridge Univ. Press, 2000.
- [13] W. K. H. Panofsky, *Classical Electricity and Magnetism*. Reading, MA: Addison-Wesley, 1962.
- [14] D. E. Goldberg, *Genetic Algorithms in Search, Optimization and Machine Learning*. Reading, MA: Addison-Wesley, 1989.
- [15] C. W. Ueberhuber, "Numerical computation," in *Minimization Methods*. Berlin, Germany: Springer, 1997, vol. 2, ch. 14, sec. 4.4, pp. 325–335.
- [16] I. J. Won, D. A. Keiswetter, and D. R. Hanson, "GEM-3: A monostatic broadband electromagnetic induction sensor," *J. Environ. Eng. Geophys.*, vol. 2, pp. 53–64, Mar. 1997.

Yan Zhang was born in Changchun, China, in 1972. He received the B.S., M.S., and Ph.D. degrees in electrical engineering from Jilin University of Technology, Changchun, China, in 1993, 1996, and 1998, respectively.

Since January 1999, he has been a Postdoctoral Research Associate in the Department of Electrical and Computer Engineering, Duke University, Durham, NC. His present research interests include statistical signal processing, pattern recognition, and related applications.

Leslie Collins (M'96–SM'01) was born in Raleigh, NC. She received the B.S.E.E. degree from the University of Kentucky, Lexington and the M.S.E.E. and Ph.D. degrees in electrical engineering, both from the University of Michigan, Ann Arbor.

She was a Senior Engineer with the Westinghouse Research and Development Center, Pittsburgh, PA, from 1986 to 1990. In 1995, she became an Assistant Professor in the Electrical and Computer Engineering Department, Duke University, Durham, NC, and was promoted to Associate Professor in 2002. Her current research interests include incorporating physics-based models into statistical signal processing algorithms, and she is pursuing applications in subsurface sensing as well as enhancing speech understanding by hearing impaired individuals.

Dr. Collins is a member of the Tau Beta Pi, Eta Kappa Nu, and Sigma Xi honor societies.

Haitao Yu was born in China, in 1965. He received the Ph.D. in electrical engineering from Huazhong University of Science and Technology (HUST), Wuhan, China, in 1995.

From 1995 to 1997, he worked in the Department of Electrical Engineering, HUST as a Research Associate. In 1997, he became an Associate Professor at HUST. From 1998 to 2001, he worked as a Research Associate in the Department of Electrical Engineering, Duke University, Durham, NC. He is currently a Research Associate in the Department of Computing and Software, McMaster University, Hamilton, ON, Canada. His research interests are computational electromagnetics in low- and high-frequency 3-D adaptive mesh generation.



Carl E. Baum (S'62–M'63–SM'78–F'84) was born in Binghamton, New York, on February 6, 1940. He received the B.S. (with honors), M.S., and Ph.D. degrees in electrical engineering from the California Institute of Technology, Pasadena, in 1962, 1963, and 1969, respectively.

He is currently a Senior Scientist at the Air Force Research Laboratory, Kirtland AFB, Albuquerque, NM. From 1963 to 1967 and from 1968 to 1971, he was stationed at the Air Force Research Laboratory, Directed Energy Directorate (formerly Phillips Laboratory, formerly Air Force Weapons Laboratory).

He has published four books: *Transient Lens Synthesis: Differential Geometry in Electromagnetic Theory* (New York: Hemisphere, 1991), *Electromagnetic Symmetry* (Washington, DC: Taylor & Francis, 1995), *Ultra-Wideband, Short-Pulse Electromagnetics 3* (New York: Plenum, 1997), and *Detection and Identification of Visually Obscured Targets* (New York: Taylor & Francis, 1998).

Dr. Baum was awarded the Air Force Research and Development Award in 1970, the AFSC Harold Brown Award in 1990, and the Air Force Research Laboratory Fellow Award in 1996. He is editor of several interagency note series on EMP (electromagnetic pulse) and related subjects and has received (1984) the Richard R. Stoddart award of the IEEE EMC Society. He is a recipient of the 1987 Harry Diamond Memorial Award, one of the IEEE Field Awards, with the citation "for outstanding contributions to the knowledge of transient phenomena in electromagnetics." He is a member of Commissions A, B, and E of the U.S. National Committee of the International Union of Radio Science (URSI). He is founder and president of SUMMA Foundation, which sponsors various electromagnetics-related activities including scientific conferences, publications, short courses, fellowships, and awards. He has led an EMP short course and HPE workshops at numerous locations around the globe.

Lawrence Carin (SM '96–F'01) was born March 25, 1963, in Washington, DC. He received the B.S., M.S., and Ph.D. degrees in electrical engineering at the University of Maryland, College Park, in 1985, 1986, and 1989, respectively.

He is currently a Professor with Duke University, Durham, NC. In 1989, he joined the Electrical Engineering Department, Polytechnic University, Brooklyn, NY, as an Assistant Professor, and in 1994 became an Associate Professor. In 1995, he joined the Electrical Engineering Department, Duke University. He was the Principal Investigator (PI) on the Multidisciplinary University Research Initiative (MURI) on demining (1996–2001), and he is currently the PI of the MURI dedicated to multimodal inversion. His current research interests include short-pulse scattering, subsurface sensing, and wave-based signal processing.

Dr. Carin is an Associate Editor of the IEEE TRANSACTIONS ON ANTENNAS AND PROPAGATION. He is a member of Tau Beta Pi and Eta Kappa Nu.